

DEVICE, Volume 3

Supplemental information

From nature's deadly strike to safety protection:

Mantis shrimp-inspired ultrafast energy

transformation for smart surveillance

Yihao Li, Yizhou Li, Yawei Wang, Mianxin Xiao, Hao Tang, Yunlong Zi, Junlei Wang, Xin Li, Wei-Hsin Liao, and Guobiao Hu

Supporting Information

Table of Contents

List of Figures

- Figure S1 Dimension details of a single MSEH and key components.
- Figure S2 Photographs of the prototyped MSEH.
- Figure S3 Exploded view of the self-locking latch and display of all components.
- Figure S5 Dimension details of a single MSEH integrated into a structure that converts the vertical excitation into horizontal force.
- Figure S6 Detailed working mechanism of the MSEH.
- Figure S7 Photographs of the single MSEH assembled in the motion converter.
- Figure S8 Dimension details of four MSEH units integrated within a larger motion converter.
- Figure S9 Photographs of the four MSEH units integrated in the motion converter.
- Figure S10 Measurement of the resistance of the coil.
- Figure S11 Photograph of the high-speed camera setup and velocity-displacement measurement test bench, along with the associated instrumentation.
- Figure S12 Time-History velocity and displacement of the magnet array during a single operational cycle with and without capacitor.
- Figure S13 Measured voltage outputs from the top and bottom coils, showing the oscillatory nature.
- Figure S14 Mesh convergence study of the finite element model in ANSYS Maxwell.
- Figure S15 The model of magnet array and coil array in Solidwork and ANSYS Maxwell.
- Figure S16 The magnetic flux density (MFD) along the Y axis of the top and bottom magnet array.
- Figure S17 Peak-to-peak and RMS voltage responses of individual coils during harvester operation.
- Figure S18 Power output characteristics of the six coils across varying load resistances.
- Figure S19 Experimental setup for identifying the critical force of a single MSEH.
- Figure S20 Operating cycle of the proposed MSEH captured during a single excitation event.
- Figure S21 Experimental setup demonstrating a single MSEH unit powering an LED array (400 LEDs) in the laboratory environment.
- Figure S22 Close-up view of the LED array under different operating states.
- Figure S23 Field demonstration of four MESH units powering multiple LED arrays (total 8000 LEDs) in the field environment.
- Figure S24 Circuit board architecture of the intelligent radar detection system.
- Figure S25 Detailed specifications of the MG58F18 radar and the operation timing diagram.
- Figure S26 Mobile application for the intelligent radar system.
- Figure S27 Real-world system deployment and hardware configuration of the intelligent radar

detection system.

Figure S28 Circuit board architecture of the ultra-low power camera system.

Figure S29 Real-time images captured using the ultra-low-power camera module.

Figure S30 Mobile application developed for the Blind Spot Safety Warning System.

Figure S31 Current, voltage, and energy consumption profile for a single image capture using the ultra-low power camera.

Figure S32 Comparison of the energy harvesting capability of the proposed MSEH with existing designs.

Figure S33 The flowchart illustrates the different operation states of the MSEH.

Figure S34 Force - displacement relationship during the loading phase - Phase II (Excitation Applied).

Figure S35 Experimental setup for identifying the critical force of the self-locking latch and the corresponding result.

Figure S36 2D cross-sectional view of the power-generating floor.

Figure S37 Conceptual illustration showing the transformation of energy between the buffer spring, magnet array, and rebound spring as the magnet array moves across the MSEH components during a single energy harvesting cycle.

List of Tables

Table S1 Detailed physical properties of the components used in the MSEH.

Table S2 Detailed physical properties of the materials used for fabricating the MSEH.

Table S3 Performance data of a single MSEH under excitations by different individuals with varying body weights (Charging capacitor 100 μ F).

Table S4 Performance data of four assembled MSEH units under vehicle load excitation at various speeds (Charging capacitor 220 μ F).

Table S5 Mesh convergence analysis parameters in ANSYS Maxwell.

Table S6 Electrical properties of the radar module.

Table S7 Summary of reported energy harvesters under low-frequency excitations.

Table S8 Summary of kinetic energy in biological and bio-inspired systems.

Table S9 The parameters of materials used in ANSYS Maxwell simulation.

Table S10 Summary of state transitions of key components across the five dynamic phases.

List of Notes

Note S1: Description of the five-phase operation and the dual-latch mechanism

Note S2: Quantitative analysis of energy flow and conversion efficiency in the five phases of MSEH operation

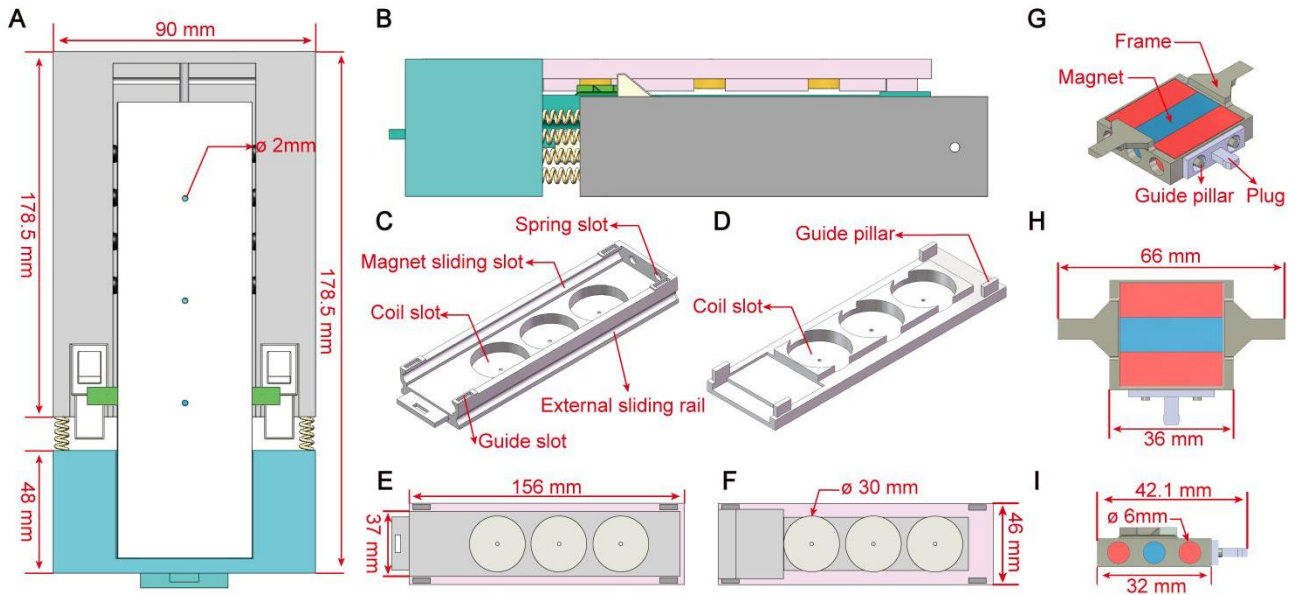


Figure S1 Dimension details of a single MSEH and key components.

- (A) Top view of the MSEH.
- (B) Side view of the MSEH.
- (C) Upper shell of the MSEH.
- (D) Lower shell of the MSEH.
- (E) Dimension details of the upper shell.
- (F) Dimension details of the lower shell.
- (G) Frame and magnet assembly with plug.
- (H) Top view of the frame and magnet assembly.
- (I) Side view of the frame and magnet assembly.

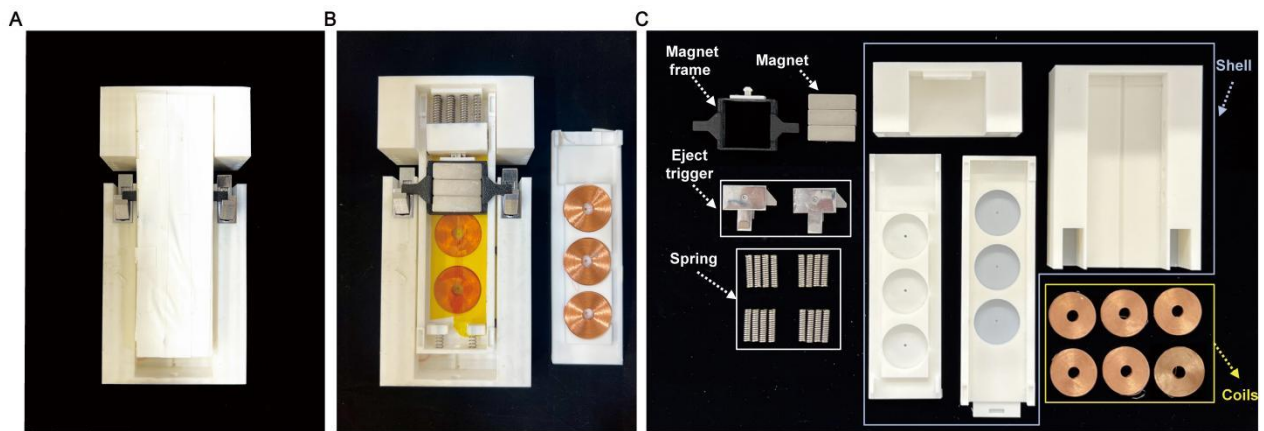


Figure S2 Photographs of the prototyped MSEH.

- (A) Top view of the MSEH.
(B) Inside view of the MSEH.
(C) Exploded view of the MSEH and display of all components.

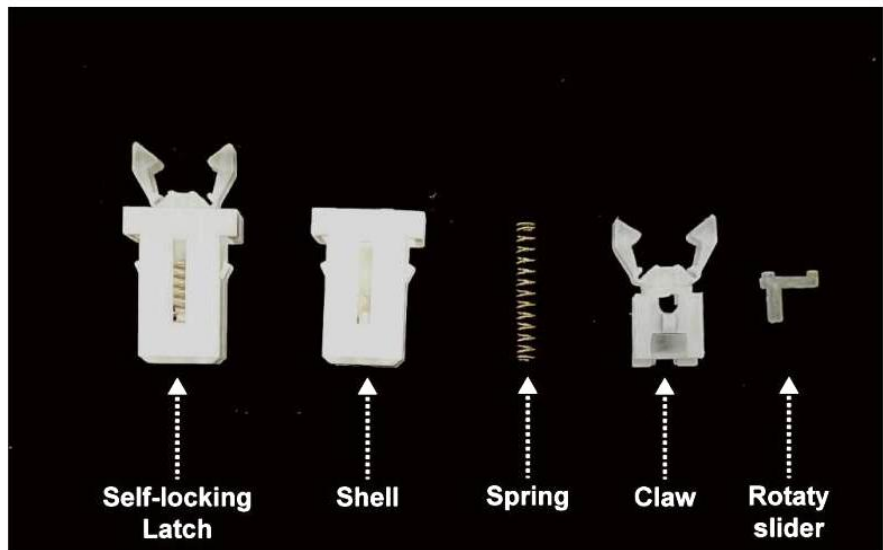


Figure S3 Exploded view of the self-locking latch and display of all components.

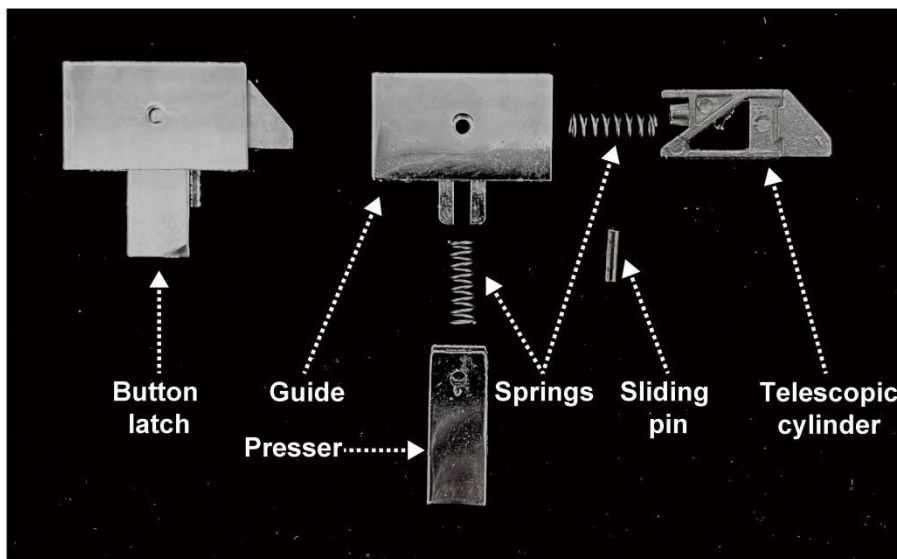


Figure S4 Exploded view of the button latch and display of all components.

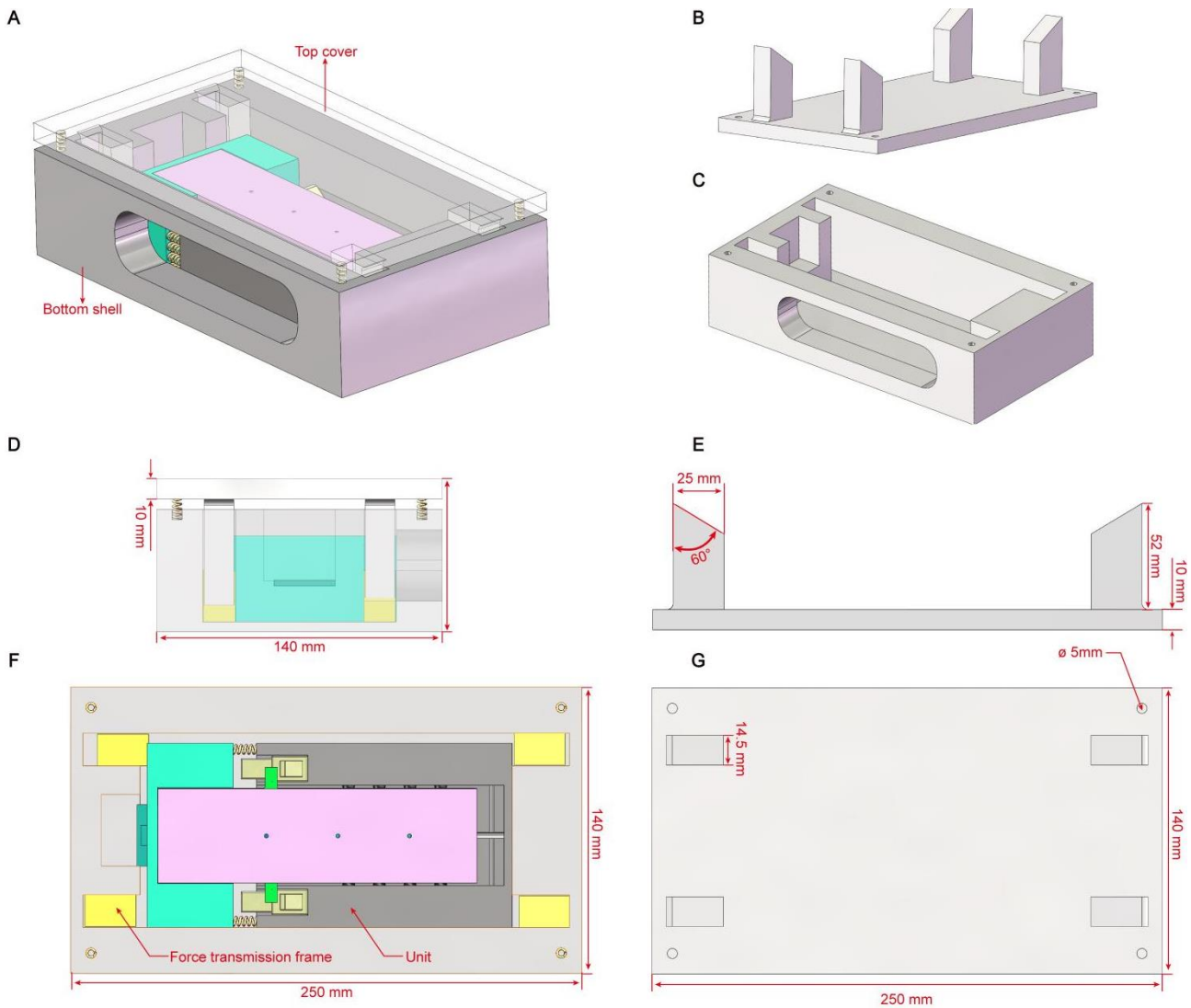


Figure S5 Dimension details of a single MSEH integrated into a structure that converts the vertical excitation into horizontal force.

- (A) Isometric view showing the installation of the single MSEH inside the motion converter.
- (B) Perspective view of the top cover (flipped state to show the detailed structure).
- (C) Structural view of the bottom housing.
- (D) The side view of the single MSEH installed in the motion converter.
- (E) The front view of the top cover.
- (F) The top view of a single MSEH installed in the motion converter without the top cover.
- (G) The top view of the top cover.

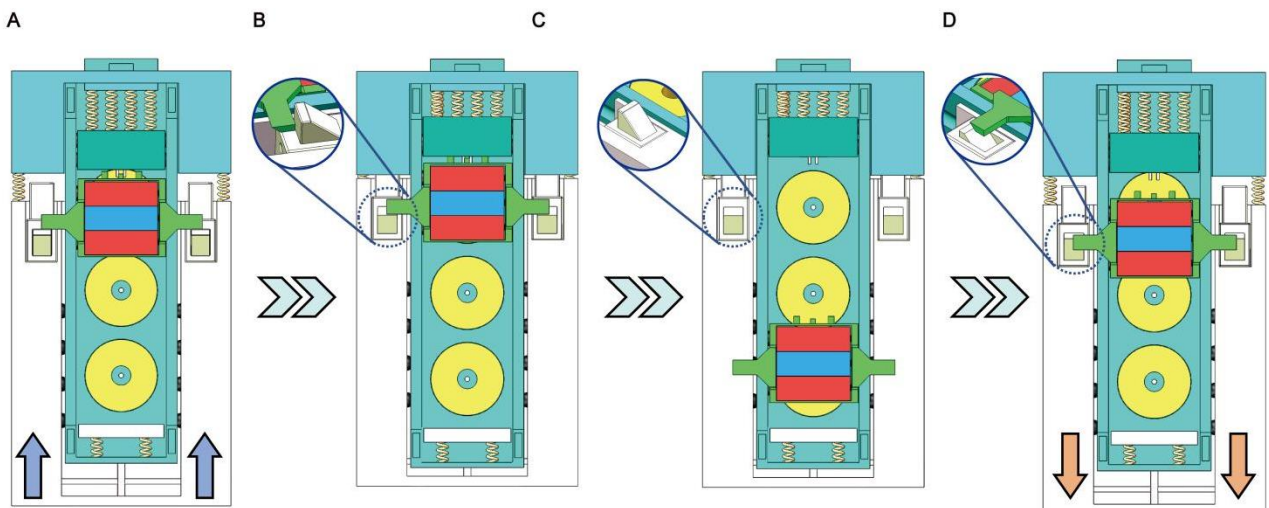


Figure S6 Detailed working mechanism of the MSEH.

- (A) Locked state the system is initially restrained by the latch mechanism, and the upward arrows indicate the applied vertical force direction.
- (B) When the applied force exceeds a threshold, the latch disengages, allowing the internal mass to shift.
- (C) The magnet array shifts downward as the buffer springs release stored energy, which is converted into the kinetic energy of the magnet array.
- (D) As the external force is withdrawn, indicated by the downward arrows, the restoring springs return the system to its initial state, relocking the magnet array and preparing it for the next excitation cycle.



Figure S7 Photographs of the single MSEH assembled in the motion converter.

- (A) Top View of the single MSEH installed in position.
- (B) Overall appearance of the single MSEH enclosed within the motion converter.
- (C) Schematic of the assembled system tested in the experiment.

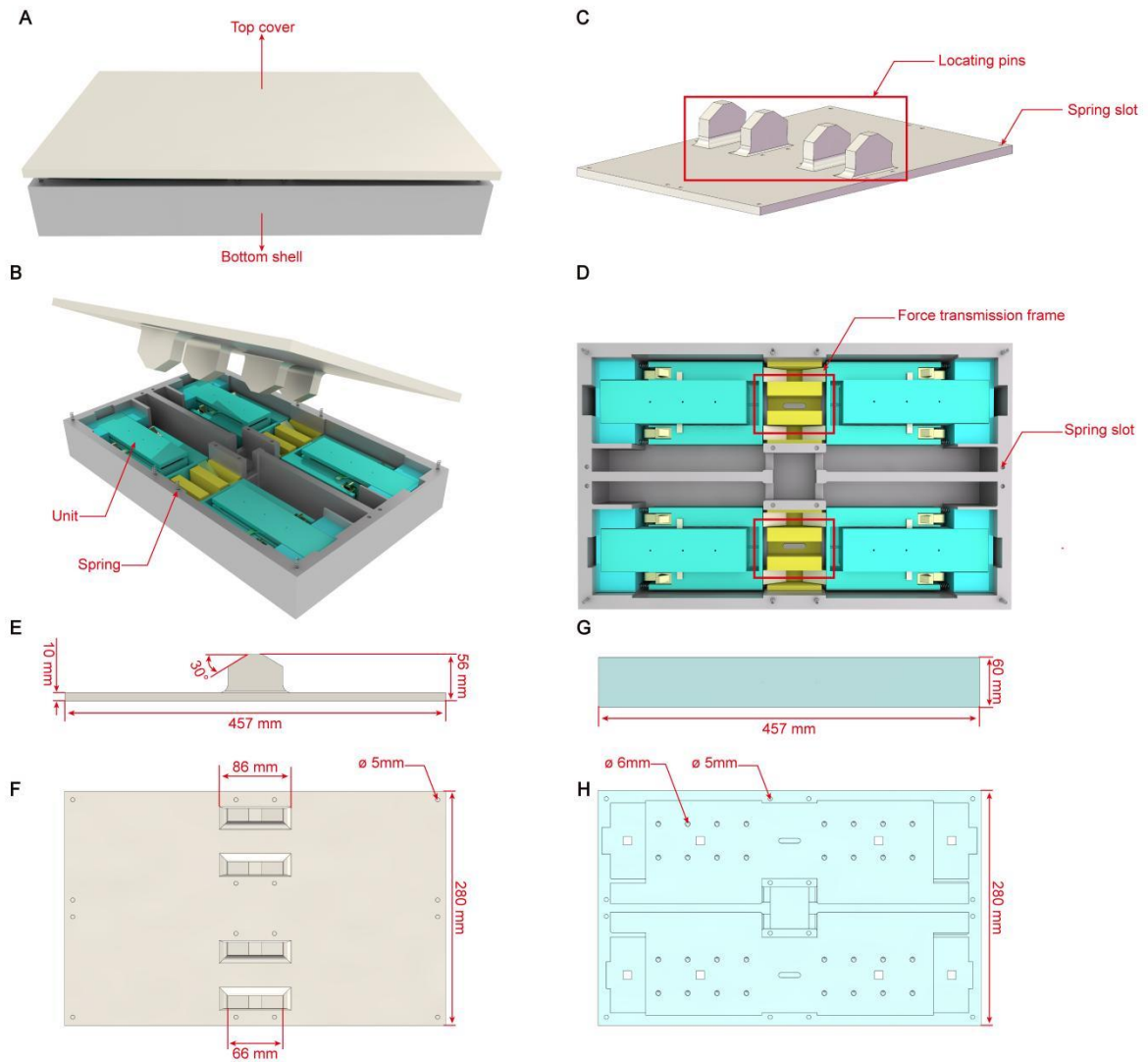


Figure S8 Dimension details of four MSEH units integrated within a larger motion converter.

- (A) External view of the four MSEH units enclosed within the large motion converter.
- (B) Illustration of the installation layout of the four MSEH units.
- (C) Structural view of the top cover.
- (D) Top view of the four MSEH units installed in the motion converter with the top cover removed.
- (E) Front view of the top cover.
- (F) Top view of the top cover.
- (G) Front view of the bottom housing.
- (H) Bottom view of the bottom housing.



Figure S9 Photographs of the four MSEH units integrated in the motion converter.

(A) Top View of the four MSEH units installed in position.

(B) Overall appearance of the four MSEH units enclosed within the motion converter.

(C) Photograph of the experimental setup, showing a vehicle driving over the motion converter with integrated MSEH units during testing.

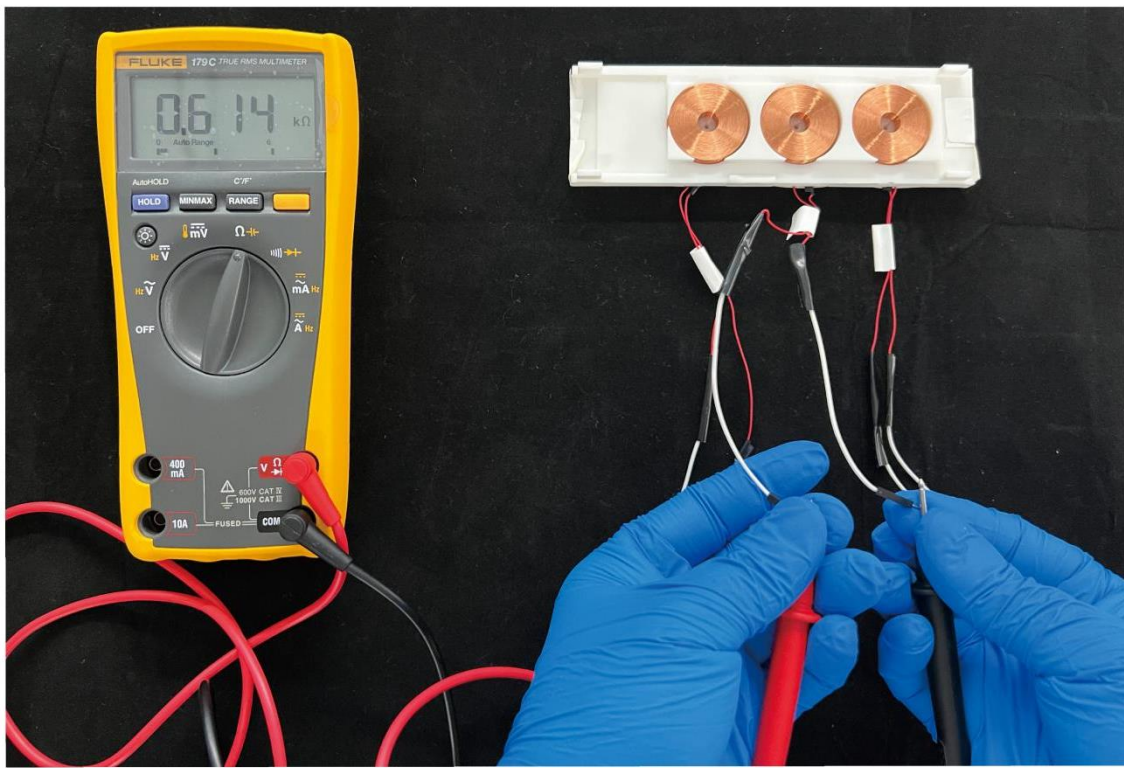


Figure S10 Measurement of the resistance of the coil.

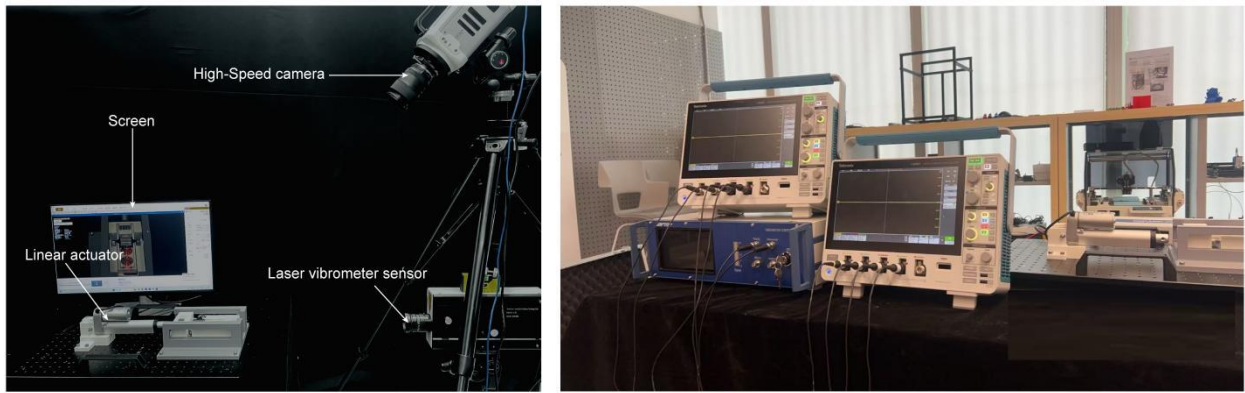


Figure S11 Photograph of the high-speed camera setup and velocity-displacement measurement test bench, along with the associated instrumentation.

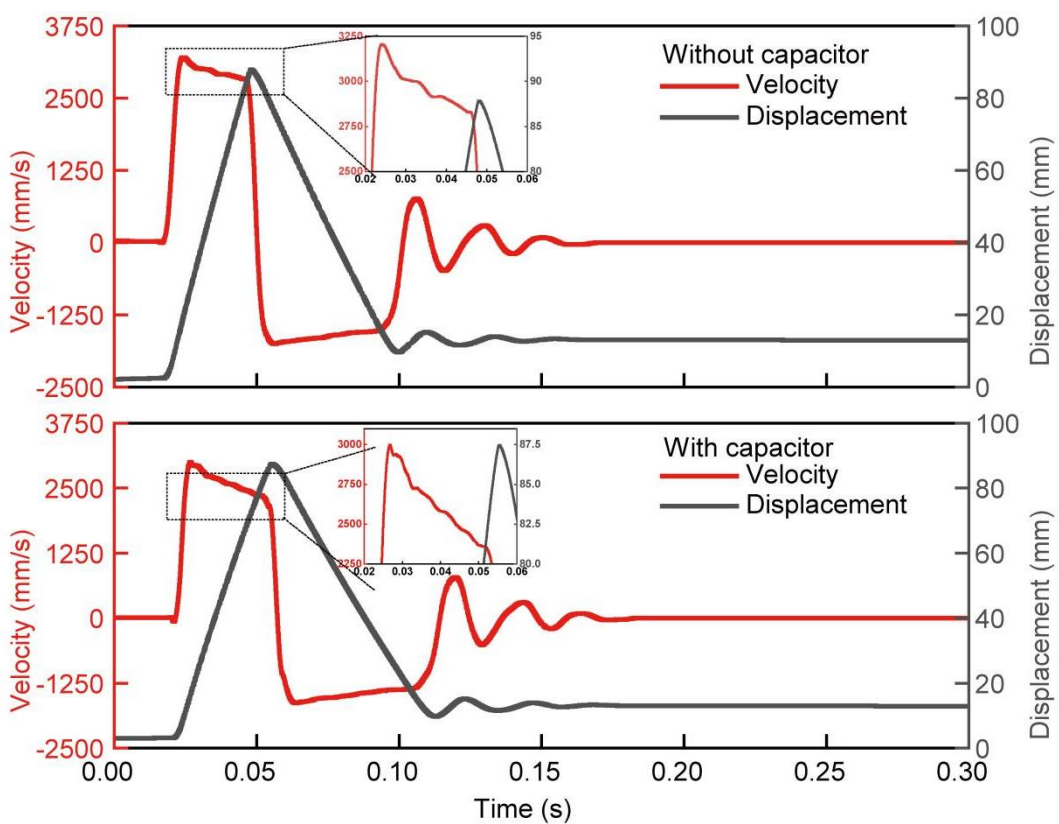


Figure S12 Time-History velocity and displacement of the magnet array during a single operational cycle with and without capacitor.

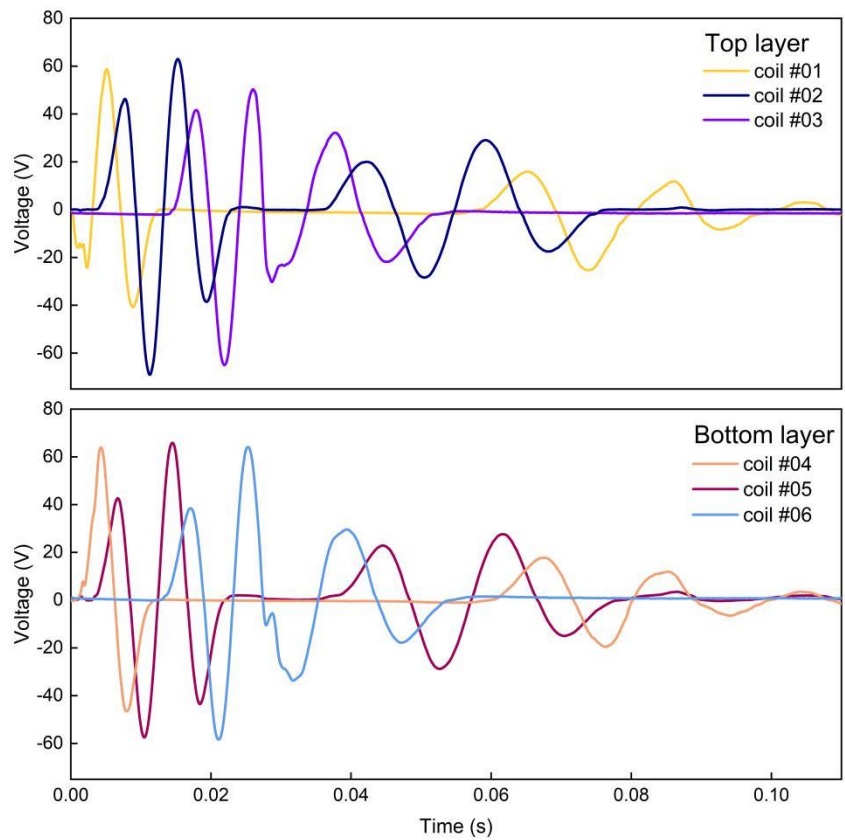


Figure S13 Measured voltage outputs from the top and bottom coils, showing the oscillatory nature.

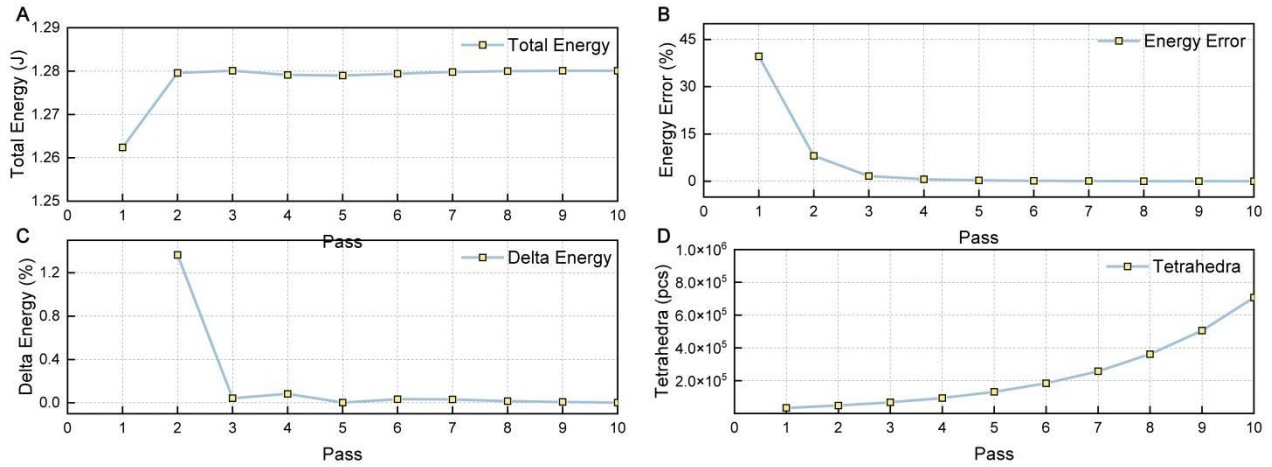


Figure S14 Mesh convergence study of the finite element model in ANSYS Maxwell.

- (A) Total energy convergence with respect to simulation passes.
- (B) Energy error percentage between consecutive passes, showing convergence behavior.
- (C) Delta energy percentage between consecutive passes.
- (D) Number of tetrahedral elements generated per simulation pass, indicating mesh density growth with refinement.

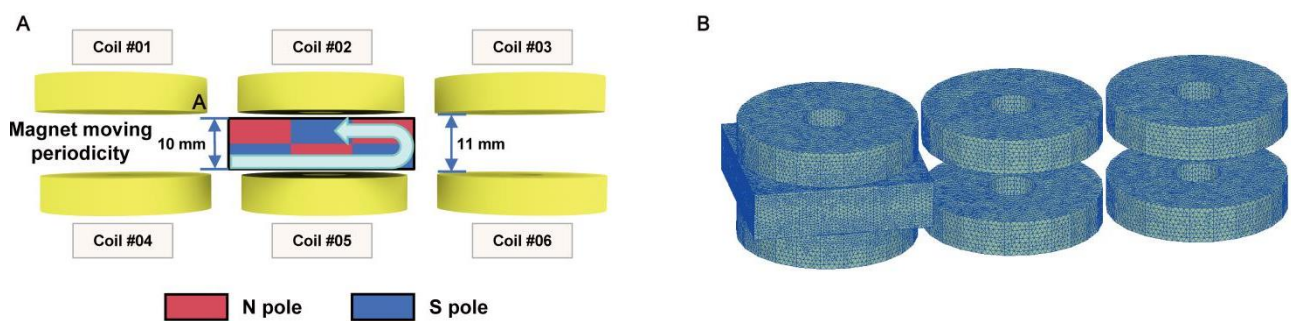


Figure S15 The model of magnet array and coil array in Solidwork and ANSYS Maxwell.

(A) The schematic diagram of the magnet array and coil array.

(B) The meshing of the magnet array and coil array.

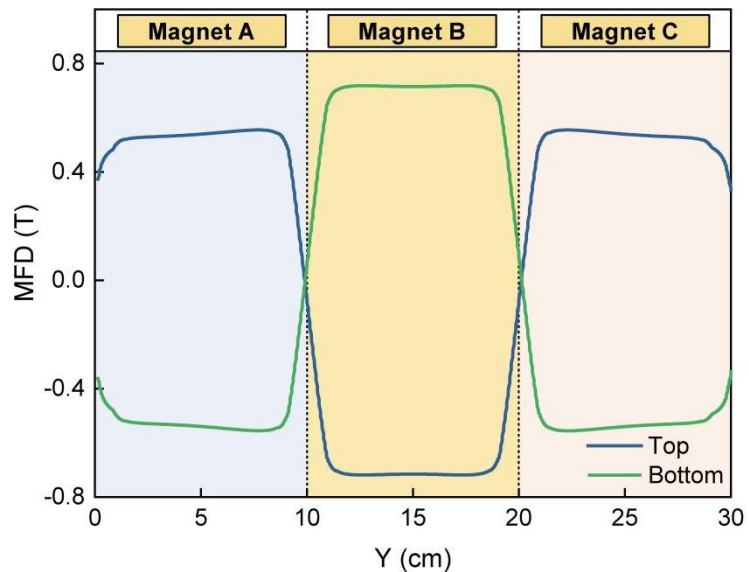


Figure S16 The magnetic flux density (MFD) along the Y axis of the top and bottom magnet array.

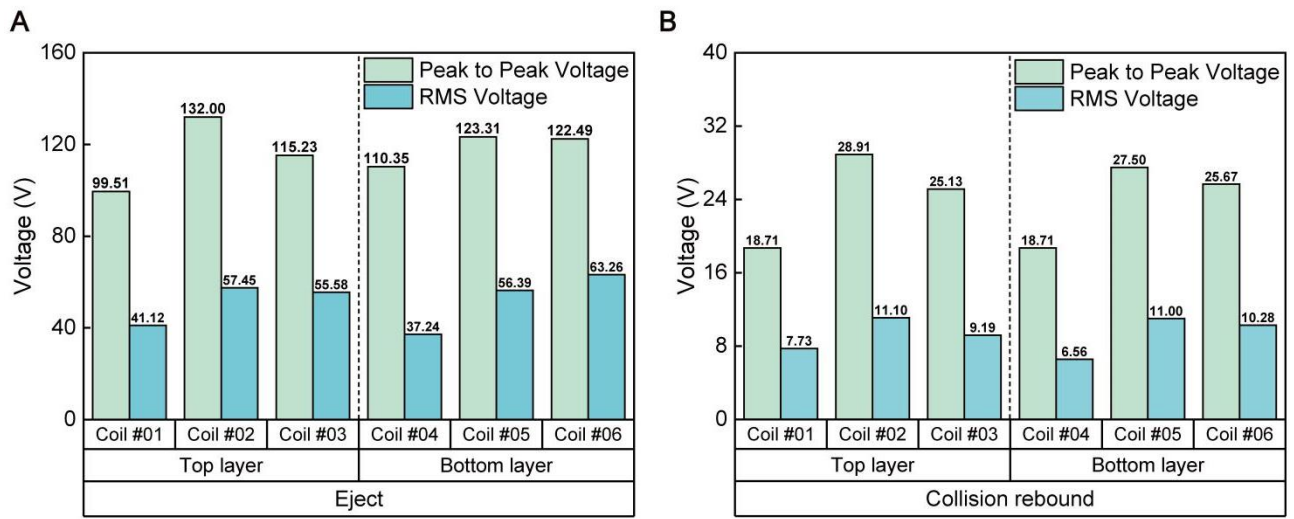


Figure S17 Peak-to-peak and RMS voltage responses of individual coils during harvester operation.

(A) Voltage output during the eject phase.

(B) Voltage output during the rebound phase after collision.

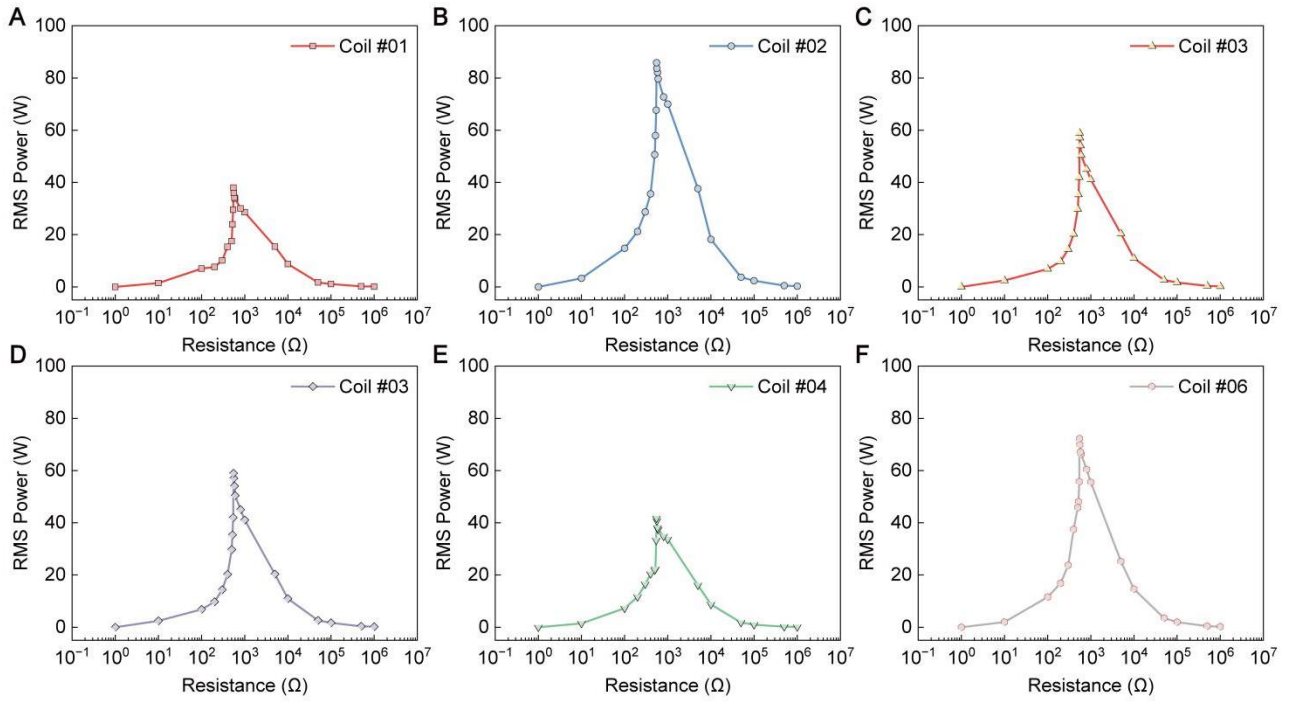


Figure S18 Power output characteristics of the six coils across varying load resistances.

(A-F) RMS power output versus resistance for Coil #01 to Coil #06, respectively.

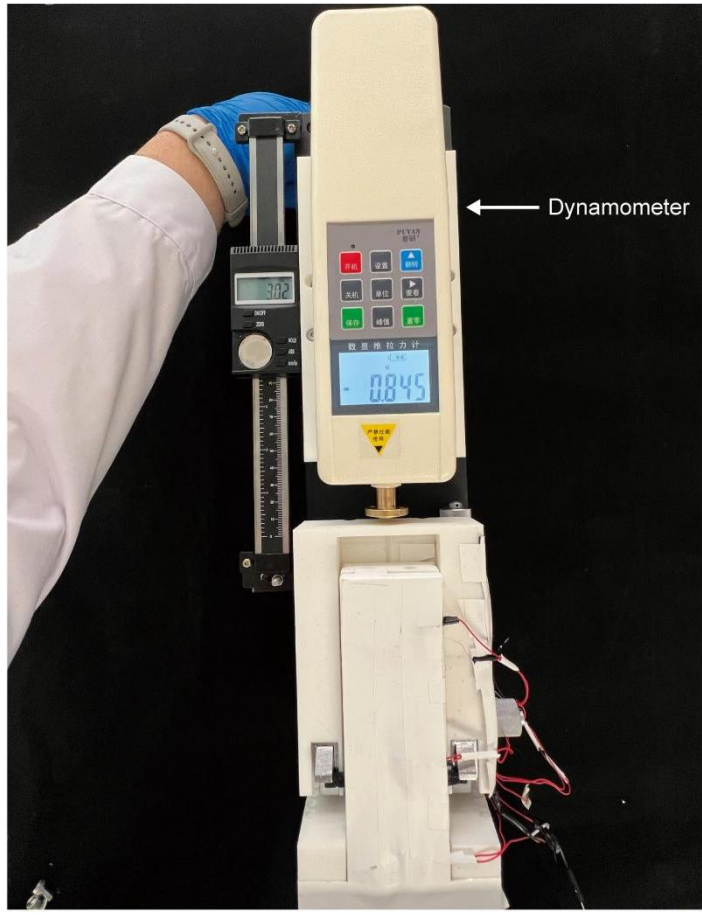


Figure S19 Experimental setup for identifying the critical force of a single MSEH.

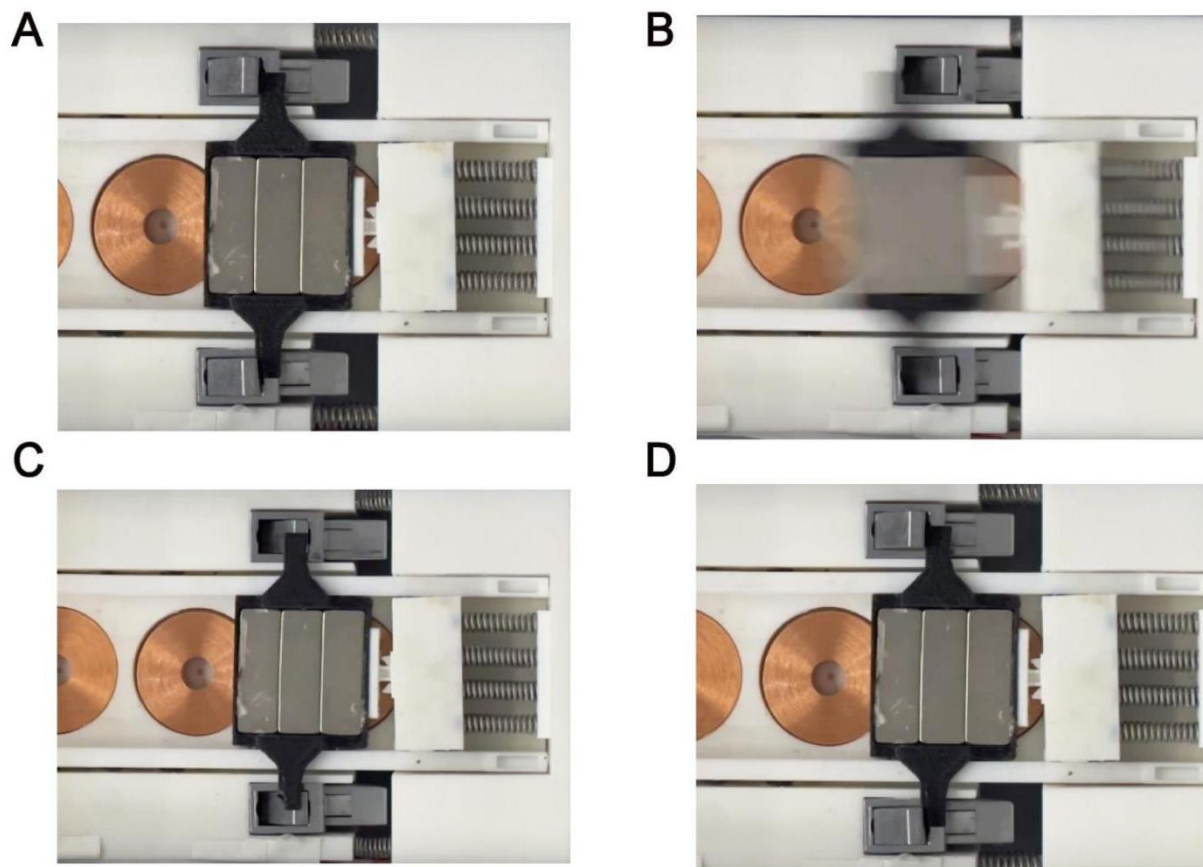


Figure S20 Operating cycle of the proposed MSEH captured during a single excitation event.

- (A) Initial stage: the system is in its rest position with the magnet array locked.
- (B) Ejection stage: the magnet array is rapidly propelled due to the accumulated energy release.
- (C) Locking stage: the magnet array reaches the end of travel and is secured by the latch mechanism.
- (D) Reset stage: restoring forces return the system to its initial state, completing the cycle.

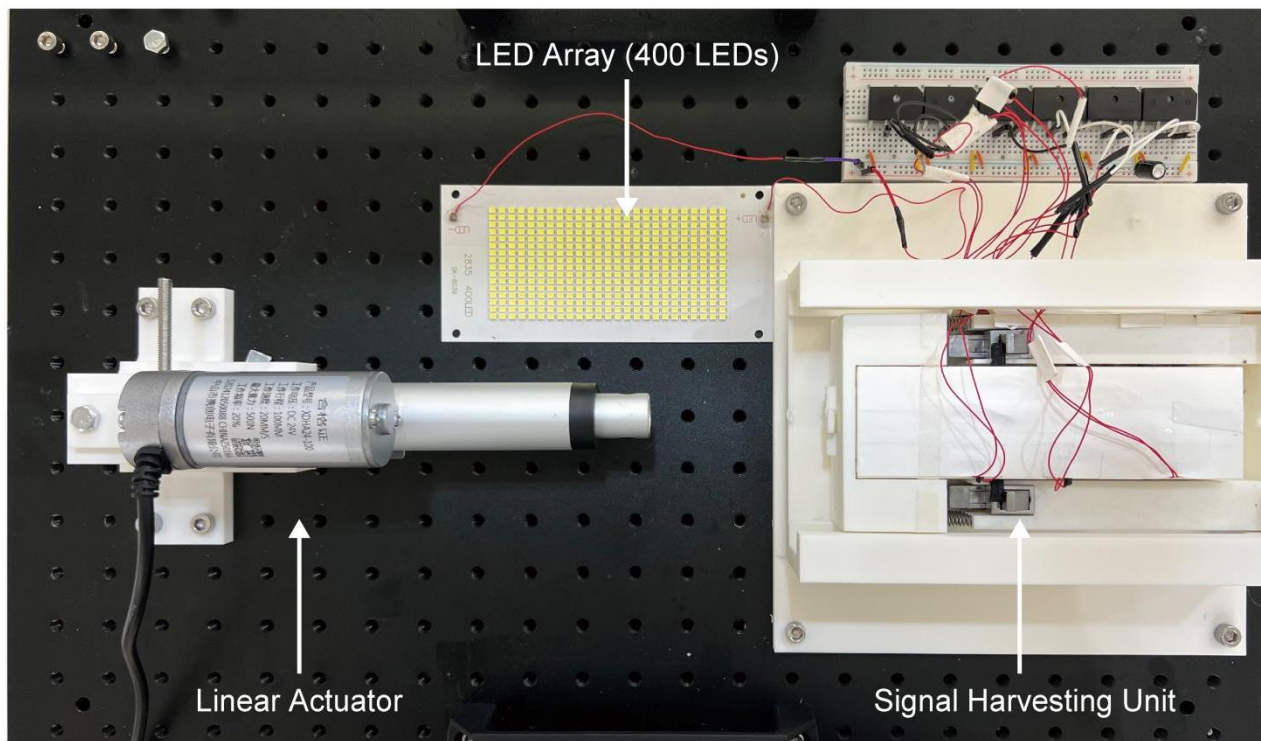


Figure S21 Experimental setup demonstrating a single MSEH unit powering an LED array (400 LEDs) in the laboratory environment.

The setup includes a linear actuator for generating repeatable excitation, a signal MSEH unit, and a 400-LED array to visually showcase the harvested energy output.

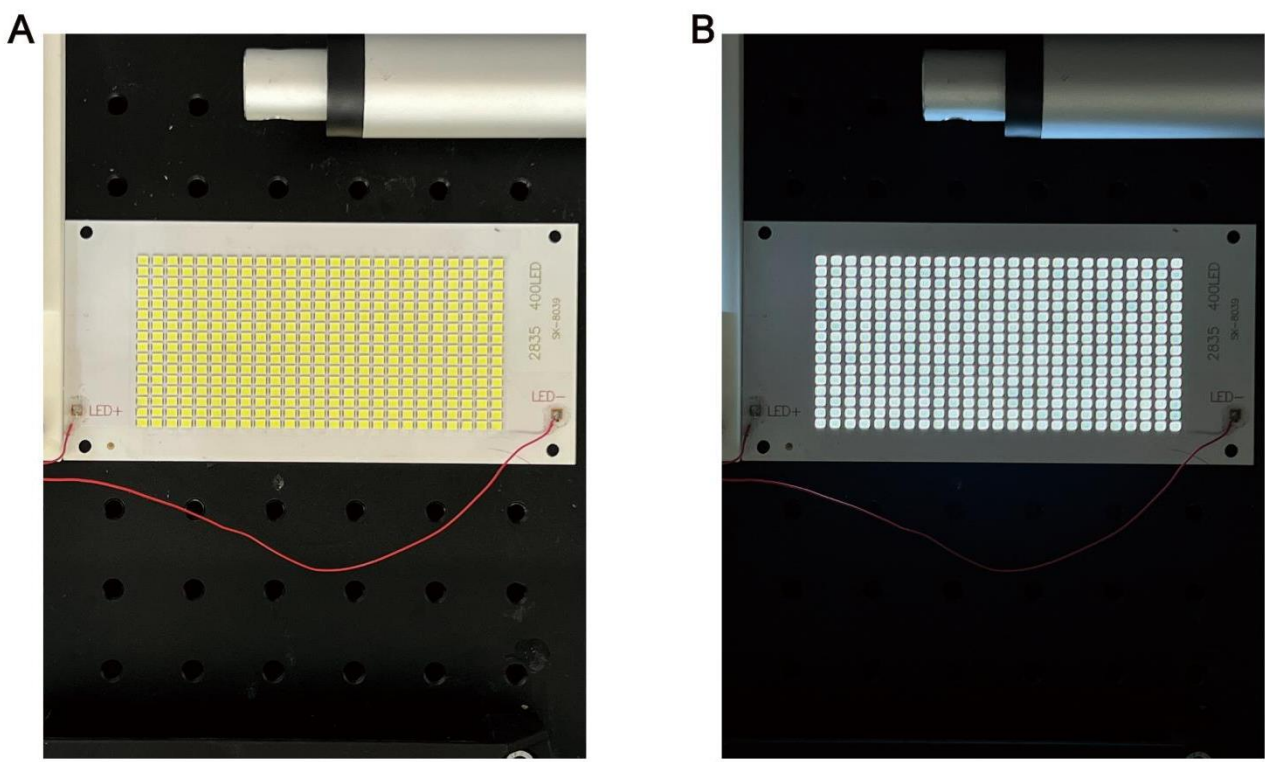


Figure S22 Close-up view of the LED array under different operating states.

(A) LEDs in the off state (no power input).

(B) LEDs illuminated, demonstrating successful energy harvesting and power delivery.

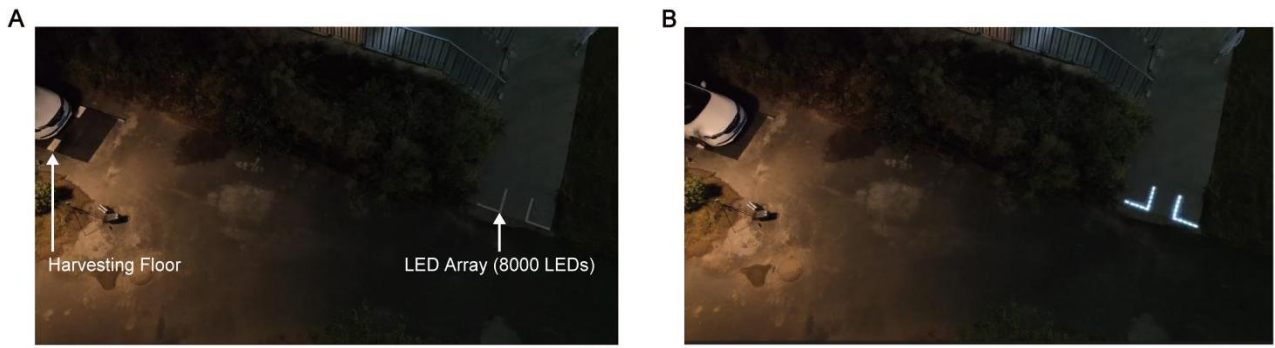


Figure S23 Field demonstration of four MESH units powering multiple LED arrays (total 8000 LEDs) in the field environment.

(A) LEDs in the off state.

(B) LEDs illuminated, showcasing the system's energy harvesting capability under real-world conditions.

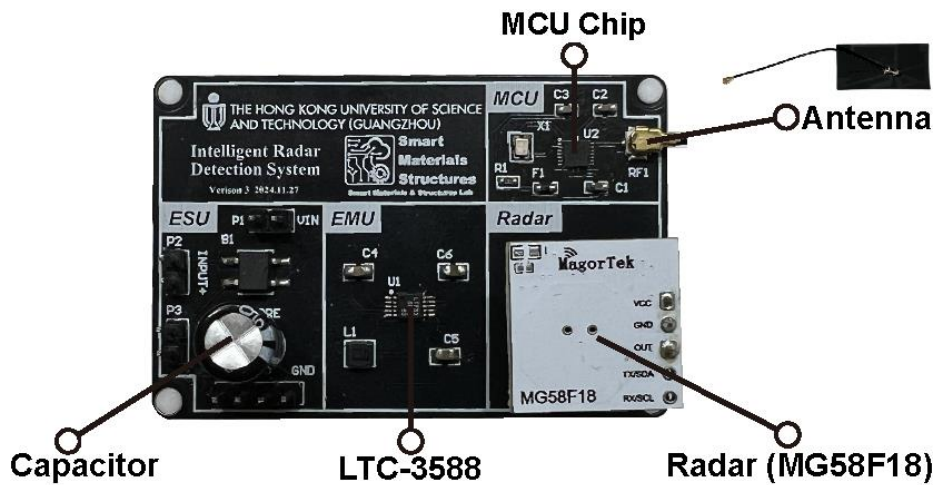


Figure S24 Circuit board architecture of the intelligent radar detection system.

Labeled components include the MCU chip, FPC antenna, radar module (MG58F18), LTC-3588 energy management unit, and supporting capacitor components, forming the core of the intelligent radar detection system.

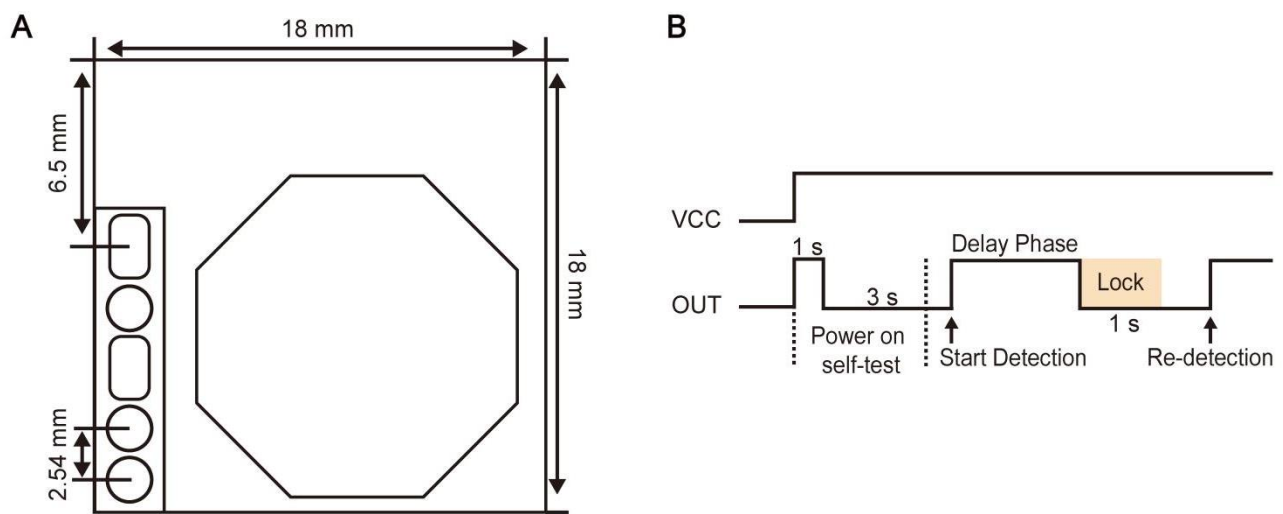


Figure S25 Detailed specifications of the MG58F18 radar and the operation timing diagram.

(A) The dimension of the MG58F18 radar module.

(B) The operation timing diagram.

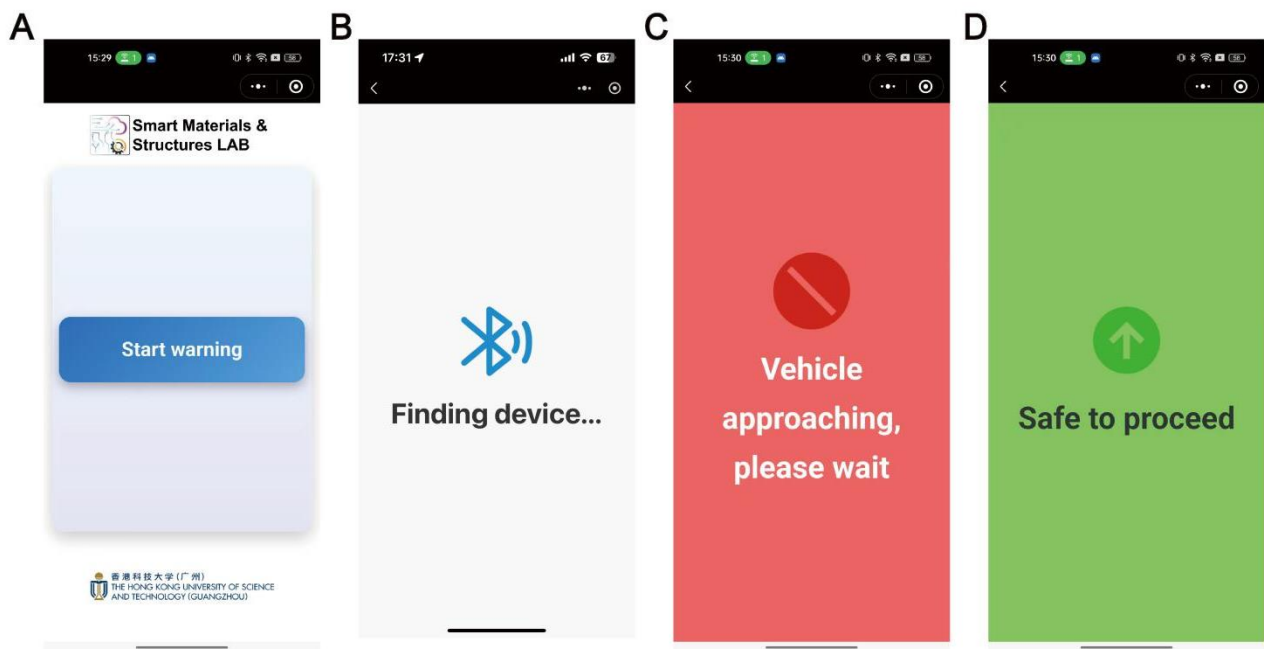


Figure S26 Mobile application for the intelligent radar system.

- (A) Home page of the mobile application showing a control button to initiate warnings.
- (B) Bluetooth module startup page indicating device pairing.
- (C) Vehicle proximity warning display.
- (D) Pedestrian-safe passage indicator when no vehicle is detected.

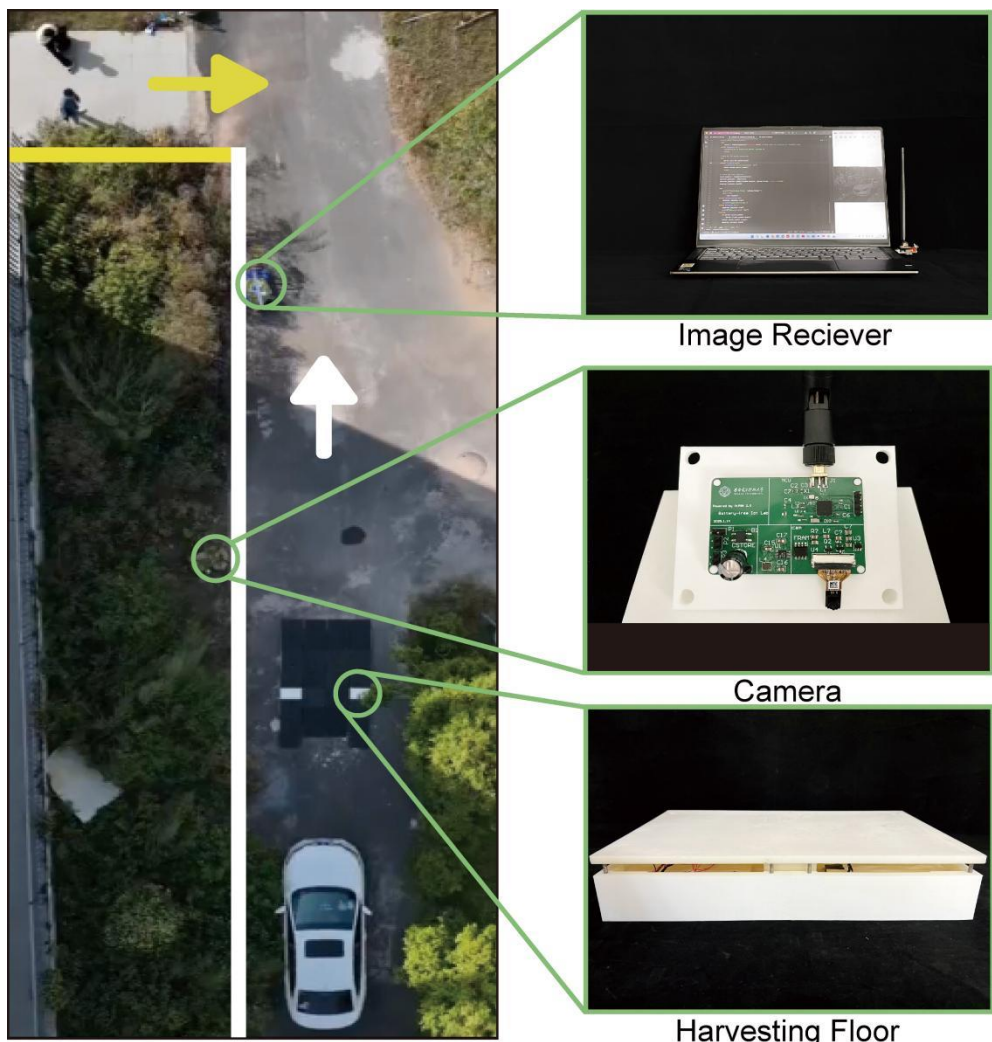


Figure S27 Real-world system deployment and hardware configuration of the intelligent radar detection system.

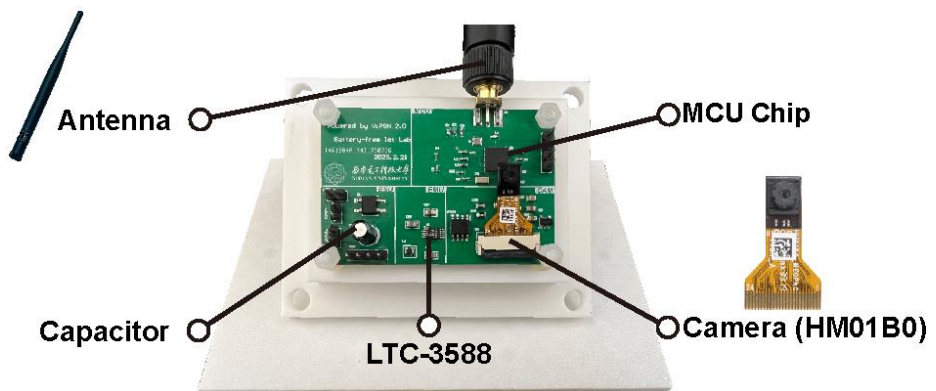


Figure S28 Circuit board architecture of the ultra-low power camera system.

Labeled components include the antenna, MCU chip, HM01B0 camera, LTC-3588 energy management unit, and supporting capacitors. This module enables low-power image capture and wireless data transmission for energy-constrained applications.

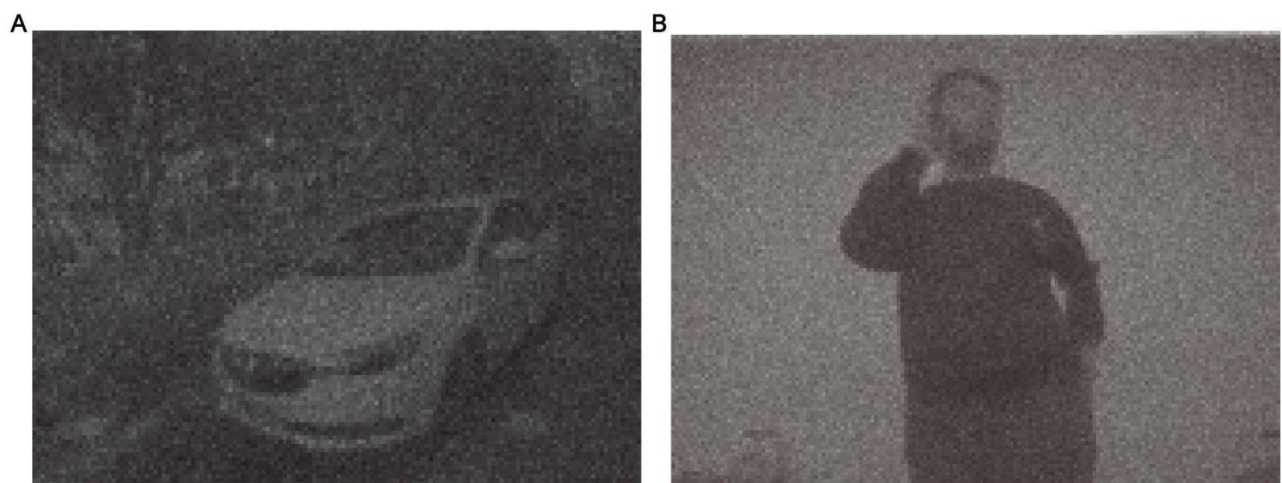


Figure S29 Real-time images captured using the ultra-low-power camera module.

- (A) Captured image of a car.
- (B) Captured image of a human.

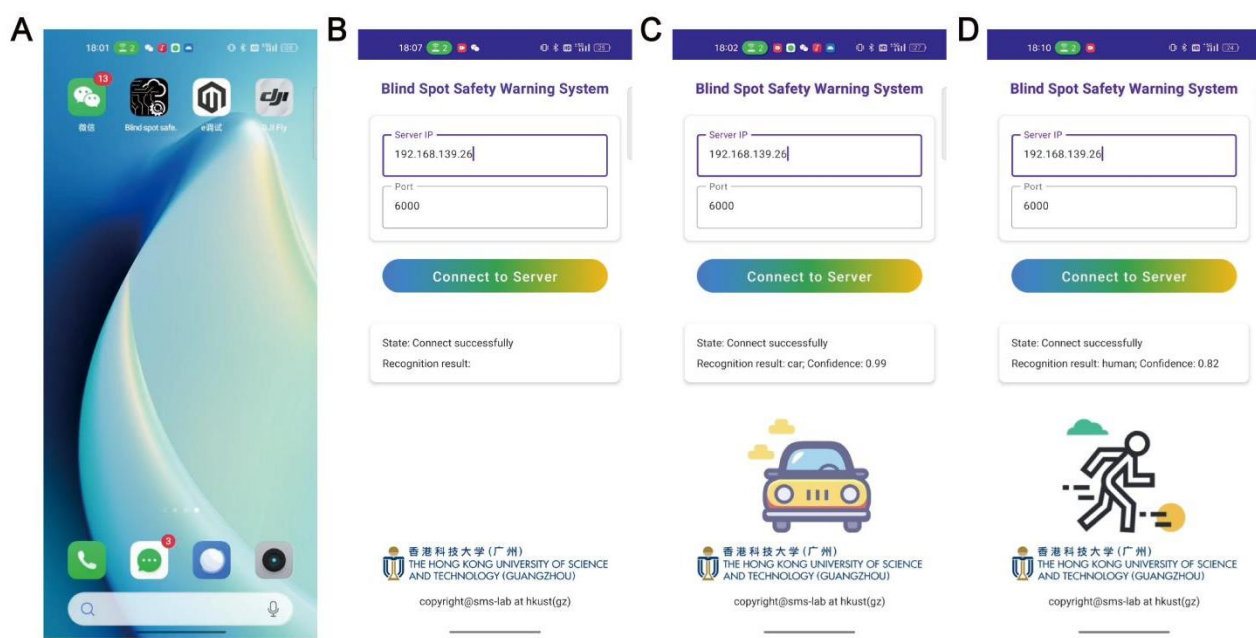


Figure S30 Mobile application developed for the Blind Spot Safety Warning System.

- (A) Smartphone home screen displaying the app icon.
- (B) App home page with server IP input interface.
- (C) Real-time vehicle recognition result with confidence level.
- (D) Real-time pedestrian recognition result with confidence level.

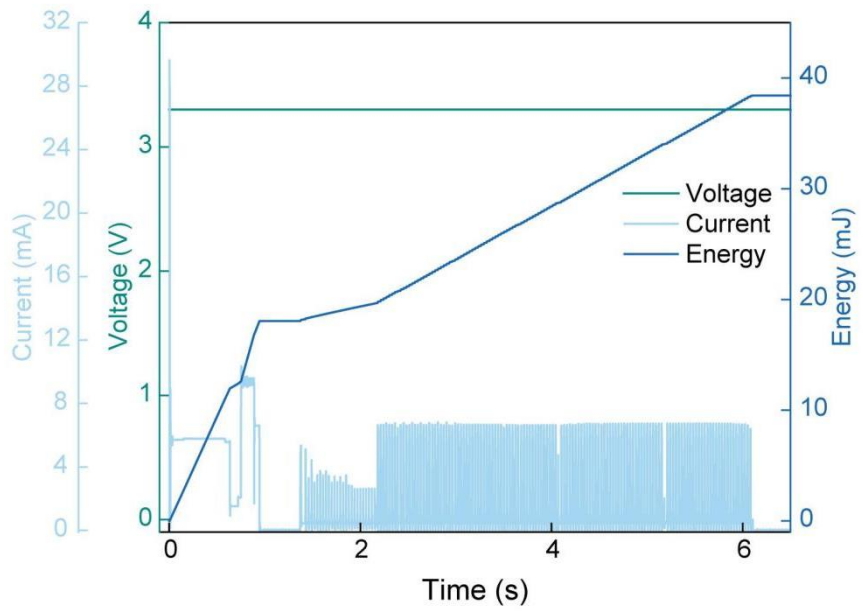


Figure S31 Current, voltage, and energy consumption profile for a single image capture using the ultra-low power camera.

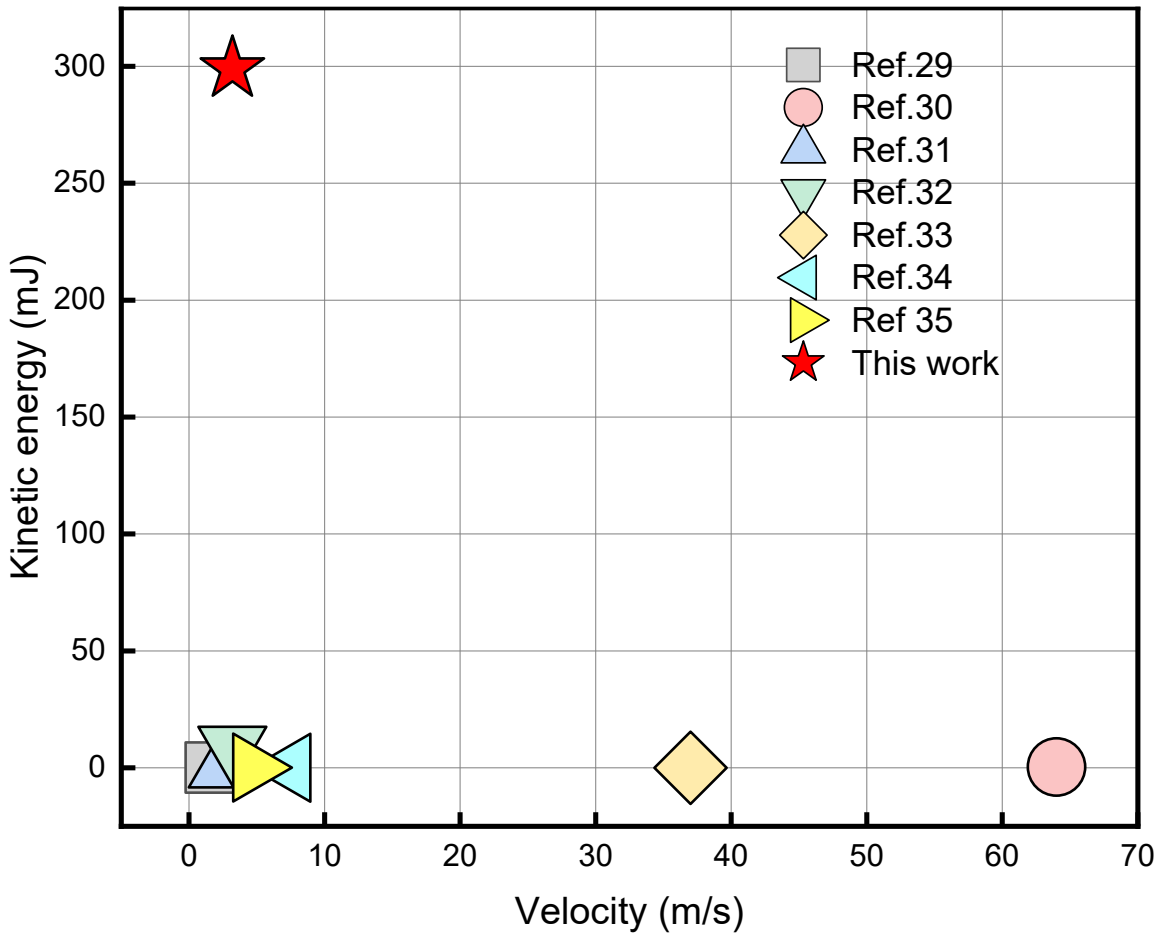


Figure S32 Comparison of the energy harvesting capability of the proposed MSEH with existing designs.

The plot highlights the superior performance of this work (red star), achieving significantly higher kinetic energy at lower velocities compared to previously reported systems (Refs. 29–35).

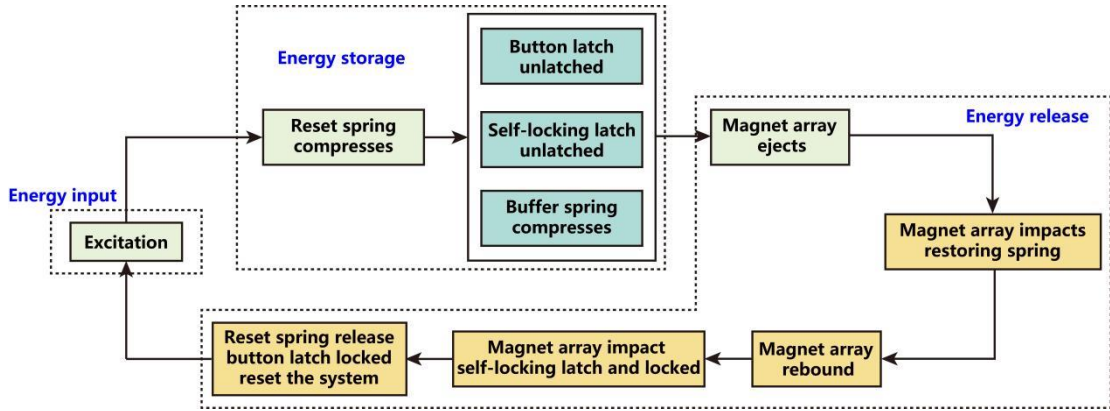


Figure S33 The flowchart illustrates the different operation states of the MSEH.

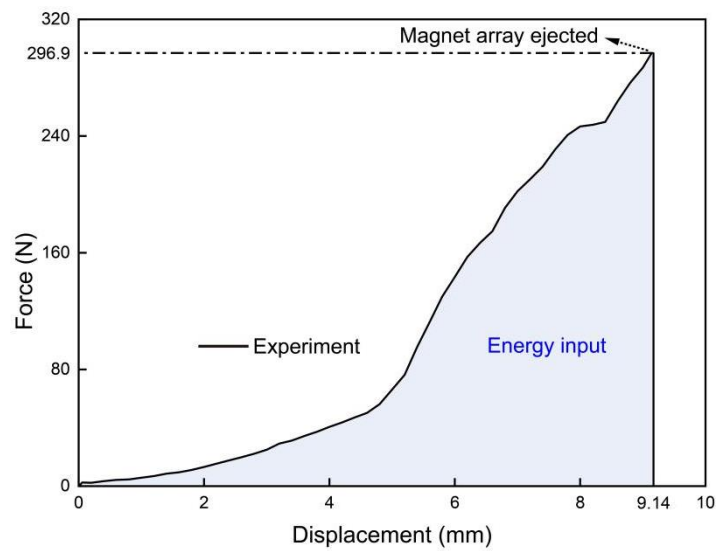


Figure S34 Force–displacement relationship during the loading phase - Phase II (Excitation Applied).

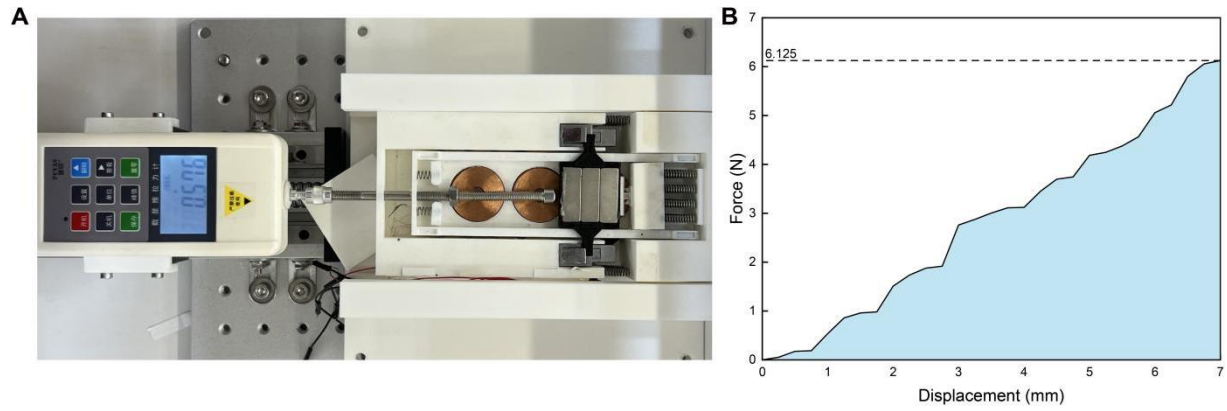


Figure S35 Experimental setup for identifying the critical force of the self-locking latch and the corresponding result.

(A) Experimental setup.

(B) Force-displacement relationship of the claw within the self-locking latch before latching.

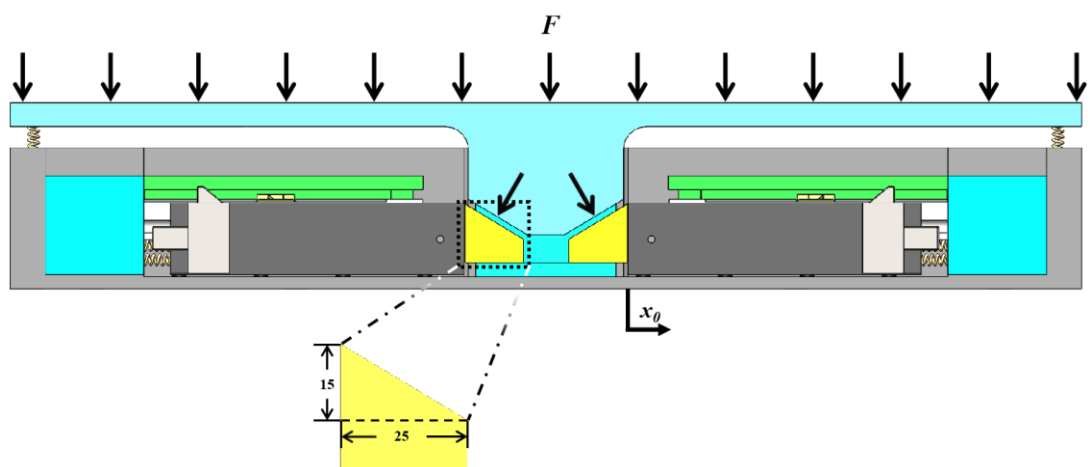


Figure S36 2D cross-sectional view of the power-generating floor.

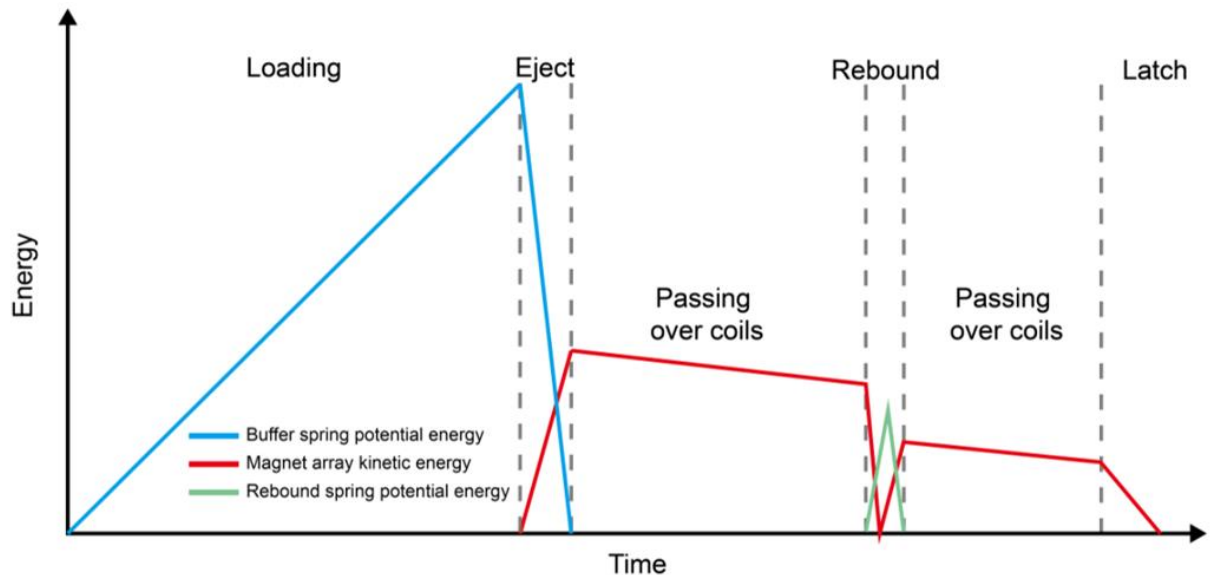


Figure S37 Conceptual illustration showing the transformation of energy between the buffer spring, magnet array, and rebound spring as the magnet array moves across the MSEH components during a single energy harvesting cycle.

Table S1 Detailed physical properties of the components used in the MSEH.

Component	Unit/Specification	Value
Release spring (UH5-20)	Stiffness (N/mm)	2.9
	External diameter (mm)	5
	Free length (mm)	20
Reset spring (UL5-15)	Stiffness (N/mm)	0.98
	External diameter (mm)	5
	Free length (mm)	15
Magnet	Quantity	3
	Magnet grade	N52
	Material	Neodymium
Magnet array	Length L (mm)	30
	Width D (mm)	30
	Thickness W (mm)	6
	B_r (T)	0.3
	Weight (g)	53
Coils	Quantity	6
	Outer diameter (mm)	30
	Inner diameter (mm)	8
	Turns	4500
	Wire diameter (mm)	0.1
	Internal resistance (Ω)	614

Table S2 Detailed physical properties of the materials used for fabricating the MSEH.

Parameter	PLA	PAHT-CF
Impact strength (XY)	26.6 kJ/m ²	57.5 kJ/m ²
Tensile strength	76 MPa	125 MPa
Tensile modulus	2750 MPa	4230 MPa
Impact strength (Z)	13.8 kJ/m ²	13.3 kJ/m ²
Heat deflection temp	57 °C	194 °C
Water absorption	0.43%	0.88%
Drying requirement	Recommended drying	Requires drying
Drying conditions	80 °C for 8-12 hours	80 °C for 8-12 hours
Print bed temp	90-100 °C	90-100 °C
Nozzle temp	190-230 °C	260-300 °C
Recommended nozzle size	0.2 mm / 0.4 mm / 0.6 mm / 0.8 mm	0.4 mm / 0.6 mm / 0.8 mm
Max print speed	< 300 mm/s	< 100 mm/s

Table S3 Performance data of a single MSEH under excitations by different individuals with varying body weights (Charging capacitor 100 μ F).

Participant	Energy (mJ)	Maximum Voltage (V)	Power (W)	Body Weight (kg)
1	33.92492	26.048	0.99779	84
2	37.12995	27.25067	1.09206	65
3	36.75303	27.112	1.08097	100.5
4	37.68062	27.452	1.10825	66
5	35.99424	26.83067	1.05865	75
6	35.34962	26.58933	1.03969	82.5
7	35.58757	26.67867	1.04669	74.8
8	35.56623	26.67067	1.04607	62.5
9	34.57048	26.29467	1.01678	67.3
10	33.14283	25.746	0.97479	59.4

Table S4 Performance data of four assembled MSEH units under vehicle load excitation at various speeds (Charging capacitor 220 μ F).

Speed (km/h)	Average Energy (mJ)	Maximum Voltage (V)	Power (W)
0-5	90.28334	30.6156	1.80567
5-10	93.13378	31.6297	1.86268
10-15	93.91912	31.3906	1.87838
15-20	95.23803	30.6906	1.90476

Table S5 Mesh convergence analysis parameters in ANSYS Maxwell.

Parameters	Values	Descriptions
Refinement per pass	40%	Increases mesh density by 40% each pass to capture finer geometric details.
Minimum number of passes	2	Sets a minimum of 2 passes to ensure model accuracy before checking convergence.
Minimum converged passes	1	Ensures at least one converged pass, even after meeting convergence criteria, to improve solution stability.
Maximum number of passes	10	Limits the maximum pass number to 10 to avoid unnecessary computation.
Percent error	0.1%	Sets the convergence condition with an error threshold of 0.1% to ensure calculation accuracy.

Table S6 Electrical properties of the radar module.

Parameter	Value	Parameter	Value
Frequency	5800 MHz	Operating current	68 µA-75 µA
Output power	0.2 mW-0.5 mW	Sensing distance	8 m-10 m
Input voltage	2.7 V-4.8 V	Delay time	15 s
Output high voltage	2.2 V	Light sensitivity	10 Lux
Output low voltage	0 V	Operating temperature	-30°C - 85°C

Table S7 Summary of reported energy harvesters under low-frequency excitations.

Reference	Volume	Excitation Characteristics	Average Power	Volume Power Density
Yin <i>et al.</i> [S1]	819 cm ³	1.1 - 1.5 Hz	5.81 mW	0.709 W/m ³
Zou <i>et al.</i> [S2]	5500.00 cm ³	Pedestrian (65 kg)	54 mW	98.180 W/m ³
Cai <i>et al.</i> [S3]	10.55 cm ³	0.7 - 1.3 Hz	0.151 mW	14.31 W/m ³
Liu <i>et al.</i> [S4]	5280.00 cm ³	5 Hz	7.21 mW	1.36 W/m ³
Li <i>et al.</i> [S5]	315.70 cm ³	< 1 Hz	76.37 mW	241.92 W/m ³
Zhang <i>et al.</i> [S6]	62.5 cm ³	2 - 5 Hz	0.00163 mW	140 W/m ³
Smilek <i>et al.</i> [S7]	50 cm ³	< 10 Hz	5.2mW	25 W/m ³
Malaji <i>et al.</i> [S8]	36 cm ³	2 - 4 Hz	0.25mW	19 W/m ³
This work	672.84 cm³	< 1 Hz	1260 mW	1867.41 W/m³

Table S8 Summary of kinetic energy in biological and bio-inspired systems.

Reference	Mass	Acceleration	Velocity	Kinetic Energy
Koh, Je-Sung, <i>et al.</i> [S9]	0.068 g	140 m/s ²	1.6 m/s	0.08704 mJ
Patek, S. N., <i>et al.</i> [S10]	0.00015 g	1×10^6 m/s ²	64 m/s	0.3072 mJ
Burrows, Malcolm. [S11]	0.0007 g	6.3×10^3 m/s ²	2.5 m/s	0.0021875 mJ
Bennet-Clark, H. C.[S12]	1.8 g	180 m/s ²	3.2 m/s	9.216 mJ
Nüchter, Timm, <i>et al.</i> [S13]	2.3e-9 g	5.4×10^7 m/s ²	37 m/s	1.57435E-06 mJ
Edwards, Joan, <i>et al.</i> [S14]	0.0004 g	2.4×10^4 m/s ²	7.5 m/s	0.01125 mJ
Vincent, Olivier, <i>et al.</i> [S15]	0.012 g	5.4×10^3 m/s ²	4.7 m/s	0.13254 mJ
This work	58.384 g	46 m/s²	3.2 m/s	298.92608 mJ

Table S9 The parameters of materials used in ANSYS Maxwell simulation.

Materials	Relative Permeability	Bulk Conductivity (S/m)	Magnetic Coercivity (A/m)	Internal resistance (Ω)
Copper	0.99991	5.8×10^7	0	610
NdFe52N (N-pole)	1.47	625000	-730000	/
NdFe52S (S-pole)	1.47	625000	-730000	/
Vacuum	1	0	0	/

Table S10 Summary of state transitions of key components across the five dynamic phases.

	Reset spring	Buffer spring	Rebound spring	Self-locking latch	Button latch	Magnet array
Phase I	Compress	Relax	Relax	Lock	Lock	Stationary
Phase II	Compress	Compress	Relax	Unlock	Lock	Stationary
		Compress	Relax			
Phase III	Compress	Relax	Compress	Unlock	Unlock	Moving
		Compress	Release			
Phase IV	Compress	Compress	Relax	Lock	Unlock	Oscillation
		Relax				
Phase V	Release	Relax	Relax	Lock	Lock	Stationary

Note S1: Description of the five-phase operation and the dual-latch mechanism

The five dynamic phases of the MSEH operation are delineated below:

- (1) **Phase I (Initial State):** The magnet array is securely held in position by both the self-locking latch and the button latch. This dual-latch mechanism maintains the system in a fully constrained state, ready for controlled energy loading upon external excitation.
- (2) **Phase II (Excitation Applied):** As the magnet array moves inward, it pushes against the telescopic cylinder (see **Fig. S4**) in the button latch, causing it to retract. This movement compresses the buffer springs, storing elastic potential energy. The resulting horizontal displacement also causes the claw of the self-locking latch to disengage from its locking groove, transitioning the self-locking latch from a 'locked' to an 'unlocked' state. At the same time, the shell presses the presser of the button latch (see **Fig. S4**), and through the action of a sliding pin, the telescopic cylinder gradually retracts inward along the guide.
- (3) **Phase III (Magnet Ejection & Return):** Upon reaching the critical displacement, the telescopic cylinder in the button latch fails to hold the magnet array in place. As a result, the stored elastic energy is rapidly unleashed and transformed into kinetic energy of the magnet array. After the release of stored energy, the magnet array decelerates, collides with the opposite shell wall, and rebounds.
- (4) **Phase IV (Relatching):** As the magnet array rebounds back and impacts the self-locking latches, it becomes engaged and securely hooked by the self-locking latch. The collision is quasi-elastic with minimal energy loss, and the weak damping effect of the internal spring of the self-locking latch causes the magnet to undergo an underdamped oscillation.
- (5) **Phase V (System Reset):** The reset spring engages upon the removal of the external force, bringing the shell and button latch back to their initial positions and readying the system for the next cycle.

Remarks on the dual-latch mechanism:

At the beginning of **Phase IV**, the rebounding magnet array impacts and re-engages the self-locking latch, which securely holds it in place. In **Phase V**, the removal of the external force triggers the engagement of the button latch, further securing the magnet array in its original position. As illustrated in **Fig. S4**, the button latch comprises a spring-loaded telescopic cylinder and a spring-loaded presser. During excitation, the presser is pushed downward by the upper housing, activating the slider pin and compressing the telescopic cylinder to release the magnet array. Once the external force is removed, the reset springs expand, restoring the presser and telescopic cylinder to their initial positions and re-locking the magnet array. The button latch serves as a secondary safety mechanism to prevent premature release before the next cycle. Because of the dual-latch configuration, removal of the external force immediately after **Phase IV** is not required for a second relatching to occur—the self-locking latch already secures the magnet array. However, displacement/force removal is essential for resetting the button latch, which completes the full operational cycle.

Note S2: Quantitative analysis of energy flow and conversion efficiency in the five phases of MSEH operation

1. Work input for spring loading and device triggering:

To quantify the mechanical input work, we have added a supplementary figure (**Fig. S34**) to further illustrate the force-displacement relationship shown in **Fig. 3D**. According to the work-energy principle, the input work corresponds to the area under the force-displacement curve. It can be calculated using the below integral:

$$W_{\text{in}} = \int_{x_0}^{x_c} F(x)dx = 917.493 \text{ mJ} \quad (2.1)$$

This work represents the total input mechanical energy. Assuming that energy losses during the slow loading process are minimal, it can be reasonably approximated as the energy stored in the buffer springs before release. Accurate quantification of this input is essential for assessing the overall energy conversion efficiency, as it serves as the baseline for comparison with the electrical output.

2. Conversion efficiency from mechanical input to kinetic energy:

Using high-speed imaging and displacement tracking (see **Fig. 2D–F**), we determined that the maximum velocity of the magnet array during ejection was approximately $v = 3.2 \text{ m/s}$. The total mass of the magnet array is about $m = 58.384 \text{ g}$ (given in **Table S8**). Therefore, the maximum kinetic energy can thus be calculated as:

$$E_k = \frac{1}{2}mv^2 = \frac{1}{2} \times 0.058384 \text{ kg} \times (3.2 \text{ m/s})^2 \approx 0.299 \text{ J} \quad (2.2)$$

Given that the total input work was calculated to be $W_{\text{in}} = 917.453 \text{ mJ}$, the mechanical-to-kinetic energy conversion efficiency is:

$$\eta_{\text{mech-kinetic}} = \frac{E_k}{W_{\text{in}}} = \frac{299 \text{ mJ}}{917.453 \text{ mJ}} \approx 32.5\% \quad (2.3)$$

This indicates that approximately 32.5% of the input mechanical energy was converted into kinetic energy by our MSEH device.

3. Electrical energy output:

As shown in **Fig. 3F**, the maximum electrical energy collected per cycle was approximately 44.24 mJ when a 100 μF capacitor was used.

4. Energy losses during ejection and return phases

While a portion of the magnet array's kinetic energy is converted into electrical energy through electromagnetic induction, several loss mechanisms reduce the overall efficiency. These include:

- i). Mechanical damping and friction in the guiding channel and ball chutes;
- ii). Elastic recoil in the buffer and restoring springs;
- iii). Impact losses during the magnet array rebound;

iv). Eddy currents and Joule heating in the coil and magnet core;

v). Residual oscillations during Phase V.

Based on the above calculation, the total kinetic energy of the magnet array is approximately 299 mJ, while the harvested electrical energy is around 44.24 mJ. The mechanical-to-electrical conversion efficiency during this stage is:

$$\eta_{\text{kinetic-electric}} = \frac{E_{\text{out}}}{E_k} = \frac{44.24 \text{ mJ}}{299 \text{ mJ}} \approx 14.8\% \quad (2.4)$$

Thus, approximately 85.2% of the kinetic energy is dissipated through the aforementioned loss pathways.

5. Overall mechanical-to-electrical energy conversion efficiency:

Combining the above stages, the overall mechanical-to-electrical conversion efficiency η of the MSEH is:

$$\eta = \frac{E_{\text{out}}}{W_{\text{in}}} = \frac{44.24 \text{ mJ}}{917.493 \text{ mJ}} \approx 4.82\% \quad (2.5)$$

This efficiency is consistent and comparable with other latch-mediated ultrafast release systems and reflects the trade-off between high-speed actuation and highly efficient energy conversion in compact architectures. Future work will focus on optimizing the mechanical structure to reduce energy losses and improving the harvesting circuit to boost power output, thereby enhancing overall system efficiency.

Supplemental Reference List

- [S1].Yin, P., Tang, L., Li, Z., Xia, C., Li, Z., and Aw, K.C. (2025). Harnessing ultra-low-frequency vibration energy by a rolling-swing electromagnetic energy harvester with counter-rotations. *Appl. Energy* 377, 124507. <https://www.doi.org/10.1016/j.apenergy.2024.124507>.
- [S2].Zou, H.-X., Zhu, Q.-W., He, J.-Y., Zhao, L.-C., Wei, K.-X., Zhang, W.-M., Du, R.-H., and Liu, S. (2024). Energy harvesting floor using sustained-release regulation mechanism for self-powered traffic management. *Appl. Energy* 353, 122082. <https://www.doi.org/10.1016/j.apenergy.2023.122082>.
- [S3].Cai, M.J., and Liao, W.H. (2021). Enhanced electromagnetic wrist-worn energy harvester using repulsive magnetic spring. *Mechanical Systems and Signal Processing* 150, 107251. <https://www.doi.org/10.1016/j.ymssp.2020.107251>.
- [S4].Liu, S., Liao, S., Liu, D., Qing, W., Wei, K., Zhao, L., and Zou, H. (2024). A compact hybridized triboelectric-electromagnetic road energy harvester for vehicle speed measurement. *DeCarbon* 3, 100036. <https://www.doi.org/10.1016/j.decarb.2024.100036>.
- [S5].Li, Y.H., Peng, X.Z., Li, Y.Z., Li, D., and Hu, G.B. (2025). Catapult mechanism-enabled push-button energy harvester designed for capturing ultra-low frequency motion. *Mechanical Systems and Signal Processing* 225, 112268. <https://www.doi.org/10.1016/j.ymssp.2024.112268>.
- [S6].Zhang, K., Wang, X., Yang, Y., and Wang, Z.L. (2015). Hybridized electromagnetic-triboelectric nanogenerator for scavenging biomechanical energy for sustainably powering wearable electronics. *ACS Nano* 9, 3521-3529. <https://www.doi.org/10.1021/nn507455f>.
- [S7].Smilek, J., Hadas, Z., Vetiska, J., and Beeby, S. (2019). Rolling mass energy harvester for very low frequency of input vibrations. *Mechanical Systems and Signal Processing* 125, 215-228. <https://www.doi.org/10.1016/j.ymssp.2018.05.062>.
- [S8].Malaji, P.V., and Ali, S.F. (2018). Analysis and experiment of magneto-mechanically coupled harvesters. *Mechanical Systems and Signal Processing* 108, 304-316. <https://www.doi.org/10.1016/j.ymssp.2018.02.025>.
- [S9].Koh, J.S., Yang, E., Jung, G.P., Jung, S.P., Son, J.H., Lee, S.I., Jablonski, P.G., Wood, R.J., Kim, H.Y., and Cho, K.J. (2015). BIOMECHANICS. Jumping on water: Surface tension-dominated jumping of water striders and robotic insects. *Science* 349, 517-521. <https://www.doi.org/10.1126/science.aab1637>.
- [S10].Patek, S.N., Baio, J.E., Fisher, B.L., and Suarez, A.V. (2006). Multifunctionality and mechanical origins: ballistic jaw propulsion in trap-jaw ants. *Proc. Natl. Acad. Sci. U. S. A.* 103, 12787-12792. <https://www.doi.org/10.1073/pnas.0604290103>.
- [S11].Burrows, M. (2012). Jumping mechanisms in jumping plant lice (Hemiptera, Sternorrhyncha, Psyllidae). *J. Exp. Biol.* 215, 3612-3621. <https://www.doi.org/10.1242/jeb.074682>.
- [S12].Bennet-Clark, H.C. (1975). The energetics of the jump of the locust *Schistocerca gregaria*. *J. Exp. Biol.* 63, 53-83. <https://www.doi.org/10.1242/jeb.63.1.53>.
- [S13].Nuchter, T., Benoit, M., Engel, U., Ozbek, S., and Holstein, T.W. (2006). Nanosecond-scale kinetics of nematocyst discharge. *Curr. Biol.* 16, R316-318. <https://www.doi.org/10.1016/j.cub.2006.03.089>.
- [S14].Edwards, J., Whitaker, D., Klionsky, S., and Laskowski, M.J. (2005). Botany: a record-breaking pollen catapult. *Nature* 435, 164. <https://www.doi.org/10.1038/435164a>.
- [S15].Vincent, O., Weisskopf, C., Poppinga, S., Masselter, T., Speck, T., Joyeux, M., Quilliet, C., and Marmottant, P. (2011). Ultra-fast underwater suction traps. *Proc. Biol. Sci.* 278, 2909-2914. <https://www.doi.org/10.1098/rspb.2010.2292>.